

The Nature of a Cosmic-ray Accelerator CTB37B Observed with Suzaku and Chandra

Ryoko NAKAMURA, Aya BAMBA, Manabu ISHIDA

Institute of Space and Astronautical Science/JAXA,

3-1-1 Yoshinodai, Sagamihara, Kanagawa 229-8510

nakamura@astro.isas.jaxa.jp, bamba@astro.isas.jaxa.jp, ishida@astro.isas.jaxa.jp

Hiroshi NAKAJIMA

Department of Physics, Graduate School of Science, Kyoto University

Kita-Shirakawa, Sakyo-ku, Kyoto 606-8502

Ryo YAMAZAKI

Department of Physical Science, Hiroshima University,

Higashi-Hiroshima, Hiroshima 739-8526

Yukikatsu TERADA

Department of Physics, Saitama University

255 Shimo-Okubo, Sakura, Saitama 338-8570

and

Gerd PÜHLHOFER, Stefan J. WAGNER

Landessternwarte, Universität Heidelberg,

Königstuhl, 69117 Heidelberg, Germany

(Received <reception date>; accepted <acceptation date>)

Abstract

We report the Suzaku and Chandra observations of the young supernova remnant (SNR) CTB37B from which TeV γ -rays are detected by the H.E.S.S. Cherenkov telescope. The 80 ks Suzaku observation provided us with a clear image of diffuse emission and high quality spectra. The spectra revealed that the diffuse emission comprises of thermal and non-thermal components. The thermal component can be represented by an NEI model with a temperature, a pre-shock electron density and an age of 0.9 ± 0.2 keV, 0.4 ± 0.1 cm⁻³ and 650_{-300}^{+2500} yr, respectively. This suggests that the explosion of CTB37B occurred in a low density space. The non-thermal power-law component was found from the southern region of CTB37B. Its photon index of ~ 1.5 and a high roll-off energy ($\gtrsim 15$ keV) indicate efficient cosmic-ray acceleration. Comparison of this X-ray spectrum with the TeV γ -ray spectrum leads us to conclude that the TeV γ -ray emission seems to be powered through either multi-zone Inverse Compton scattering or the decay of neutral pions. The point source resolved by Chandra near the shell is probably associated with CTB37B because

of the common hydrogen column density with the diffuse thermal emission. Spectral and temporal characteristics suggest that this source is a new anomalous X-ray pulsar.

Key words: acceleration of particles — ISM: individual (CTB37B) — ISM: supernova remnants — X-rays: ISM

1. Introduction

Supernova Remnants (SNRs) are one of the most promising acceleration sites of cosmic rays. In fact, ASCA detected synchrotron X-ray emission from the shell of SN 1006, which unambiguously indicates the acceleration of electrons up to ~ 100 TeV (Koyama et al. 1995). Following this discovery, the synchrotron X-ray emission has been discovered from a shell of a few more SNRs, such as RX J1713.7–3946 (Koyama et al. 1997) and RCW 86 (Bamba et al. 2000). On the other hand, TeV γ -rays have also been detected from some non-thermal shell-type SNRs. The radiation of TeV γ -ray is explained by either (1) Inverse-Compton scattering (IC) of cosmic microwave background photons by the same high energy electron giving rise to the X-ray synchrotron emission or (2) the decay of neutral pions that are generated by collisions between high energy protons and dense interstellar matter. The ratio of fluxes between the TeV γ -ray and the X-ray provides the magnetic field intensity as long as one assumes that the TeV γ -ray is produced through the IC mechanism. Utilizing this characteristic, Matsumoto et al. (2007) found that the TeV γ -ray from HESS J1616–508 is likely the result of the proton acceleration, because the non-detection of X-ray using the Suzaku XIS provides much weaker magnetic field than the interstellar average.

Although the evidence of particle acceleration has accumulated rapidly, our knowledge is still limited on what sort of conditions are necessary for SNRs to accelerate particles. A breakthrough may be brought about by searching SNRs from which the TeV γ -ray emission is already detected for thermal emission systematically, since the thermal emission provides us with a lot of information on the environment such as temperature, density, and age of the plasma.

CTB37B locates at $(l, b) = (348^\circ.7, +0^\circ.3)$ with a distance of 10.2 ± 3.5 kpc (Caswell et al. 1975). This region is one of the most active regions in our galaxy where star burst activities, a number of shell structures probably associated with recent SNRs (Kassim et al. 1991), and OH maser sources (Frail et al. 1996) are detected in radio band. TeV γ -ray emission is also detected by the H.E.S.S. observation (Aharonian et al. 2007). In spite of the evidence of the high activities in other wave bands, X-ray observations have been relatively poor. Only ASCA (Tanaka et al. 1994) has detected a part of CTB37B at the edge of the field of view of the Gas Imaging Spectrometer (GIS) (Ohashi et al. 1996; Makishima et al. 1996) in the course of the galactic plane survey (Sugizaki et al. 2001; Yamauchi et al. 2008). Although the statistics are limited and the response of the GIS is not qualified at the pointing position of CTB37B, Yamauchi et al. (2008) represents that the fit of a power law to the GIS spectrum results in a steep photon index of ~ 4.1 , whereas fit of an optically thin thermal plasma model requires a high temperature of ~ 1.6 keV. These results strongly suggest that the X-ray

spectrum is a mixture of a non-thermal power law and an optically thin thermal plasma emission. In addition, Aharonian et al. (2008) resolved a bright point source located near the shell of CTB37B from the diffuse emission by Chandra, although its spectral parameters are not constrained very well because of short exposure time.

In order to take an image and high quality spectra of CTB37B, we have carried out an observation of CTB37B with Suzaku. We also refer to the Chandra archival data to include the spatial structure and to compare them to our Suzaku data. In § 2, we present the observation log and data reduction method. Image analysis is presented in § 3. Spectrum analysis and timing analysis are shown in § 4 and § 5, respectively. We have really detected both the thermal and non-thermal power-law components from CTB37B. Discussions are made in § 6 on the nature of the thermal and non-thermal component as well as the point source. Finally we summarize our results in § 7.

2. Observation and Data Reduction

2.1. Suzaku Observation

CTB37B was observed with Suzaku (Mitsuda et al. 2007) during 2006 August 27–29. The nominal pointing position was (RA, Dec) = ($17^{\text{h}}13^{\text{m}}57^{\text{s}}$, $-38^{\circ}12'15''$, J2000). Suzaku is equipped with two kinds of X-ray detectors; one is the Hard X-ray Detector (HXD; Takahashi et al. 2007; Kokubun et al. 2007), which is a non-imaging type detector and is sensitive in the 10-600 keV band. The other is the X-ray Imaging Spectrometer (XIS; Koyama et al. 2007), which is an X-ray CCD camera mounted on the focal plane of the X-Ray Telescope (XRT; Serlemitsos et al. 2007). In total, there are four modules of the XIS, three of which are Front-Illuminated (FI) CCDs, which are hereafter referred to as XIS-0, 2, and 3, and the other one is a Back-Illuminated (BI) CCD, which is referred to as XIS-1. The XRT has a point-spread function (PSF) of a Maltese-cross shape with a core radius of $\sim 15''$ accompanied by an outskirt extending a few arcmin. The half-power diameter (HPD) of each telescope is ~ 2 arcmin. We concentrate on the XIS data in this paper because the HXD has no imaging capability and hence there remains a large systematic error in estimating the flux from CTB37B.

The XIS was operated in the normal full-frame clocking mode with neither burst nor window options and SCI-off. The editing mode was 3×3 in low and medium data rates and 5×5 in high and super-high data rates. In analysis, we employed the data processed with the revision 1.2 pipeline software, and used the HEADAS software (version 6.2) and XSPEC (version 11.3.2) for the data reduction and spectral analysis, respectively. We applied the charge-transfer inefficiency (CTI) correction by ourselves with the xispi software and CTI parameters of 2006–08–23. After the screening of the data, the effective exposure time of 80 ksec in total. The response matrix files (RMF) and ancillary response files (ARF) were made using xisrmfgen and xissimarfgen (Ishisaki et al. 2007) version 2007–09–22 under the assumption that the emissions are from point source.

2.2. Chandra Observation

Chandra observation was performed on the 2th February 2007 with the Advanced CCD Imaging Spectrometer (ACIS). Chips I0, I1, I2, I3 S2 and S3 were used. The angular resolution is ~ 0.5 arcsec which correspond to the CCD pixel size. The data reduction and analysis were made using the Chandra Interactive Analysis of Observations (CIAO version 3.4, CALDB version 3.3.0). The total exposure time is 26 ksec after screening the data.

3. Image Analysis

3.1. Suzaku Images

Fig. 1 shows Suzaku XIS images in 0.3–3.0 keV and 3.0–10.0 keV. They are created by combining those from all the four XIS modules and smoothed with a Gaussian with $\sigma = 12$ arcsec, which is close to the XRT core size and effective in highlighting the diffuse emission. The source that locates at $(l, b) \simeq (348^\circ 68, 0^\circ 37)$ appears as the brightest source both in the soft and hard bands. Another source extending to the south of the brightest source, at $(l, b) \simeq (348^\circ 63, 0^\circ 32)$ seems to be a diffuse source and manifests itself only in the band above 3 keV. In addition to these sources, a point source is detected at $(l, b) \simeq (348^\circ 56, 0^\circ 33)$ in the band below 3 keV. The sky position is consistent with that of the point source 1RXS J171354.4–381740 listed in the ROSAT Bright Star Catalogue (Voges et al. 1999). In order to investigate these sources separately, we defined the following photon-integration regions (see Fig. 1) for the spectral analysis. Region 1 is the green circle with a radius of $2'6$ centered at the intensity peak of the brightest source. Region 2 is the blue ellipse with a major and minor axis of $2'5$ and $1'1$, respectively, which is centered at the second diffuse source. Region 3 is the circle colored in magenta with a radius of $1'3$. The other three regions with the same colors but with dashed lines define those collecting the background events. We set these background regions by taking into account the telescope vignetting.

3.2. Chandra Images

Fig. 1(c) shows the Chandra image in the 0.3–10.0 keV band corrected for the telescope vignetting and smoothed with a Gaussian with $\sigma = 6$ arcsec to see the point sources clearly. In total, 18 sources are detected above 5σ confidence level (Aharonian et al. 2008). The panels (d) and (e) are images in 0.3–3.0 keV and 3.0–10.0 keV, respectively, after removing the point sources. They are smoothed with a Gaussian with a $\sigma = 40$ arcsec to highlight the diffuse emission. The definition of the colored regions is same as those drawn in the Suzaku images. The brightest source in region 1 is a point source, which is defined as source A, locating at $(l, b) = (348^\circ 681, 0^\circ 371)$. Although most of the flux from region 1 originates from the point source, it is revealed from Fig. 1(d) that region 1 is accompanied by a diffuse emission. These two components are mixed in the Suzaku images. As expected from the Suzaku images in Fig. 1(a) and (b), region 2 is brighter than region 1 in the band above 3 keV. In region 3, there is the second bright source (defined as source B, which is

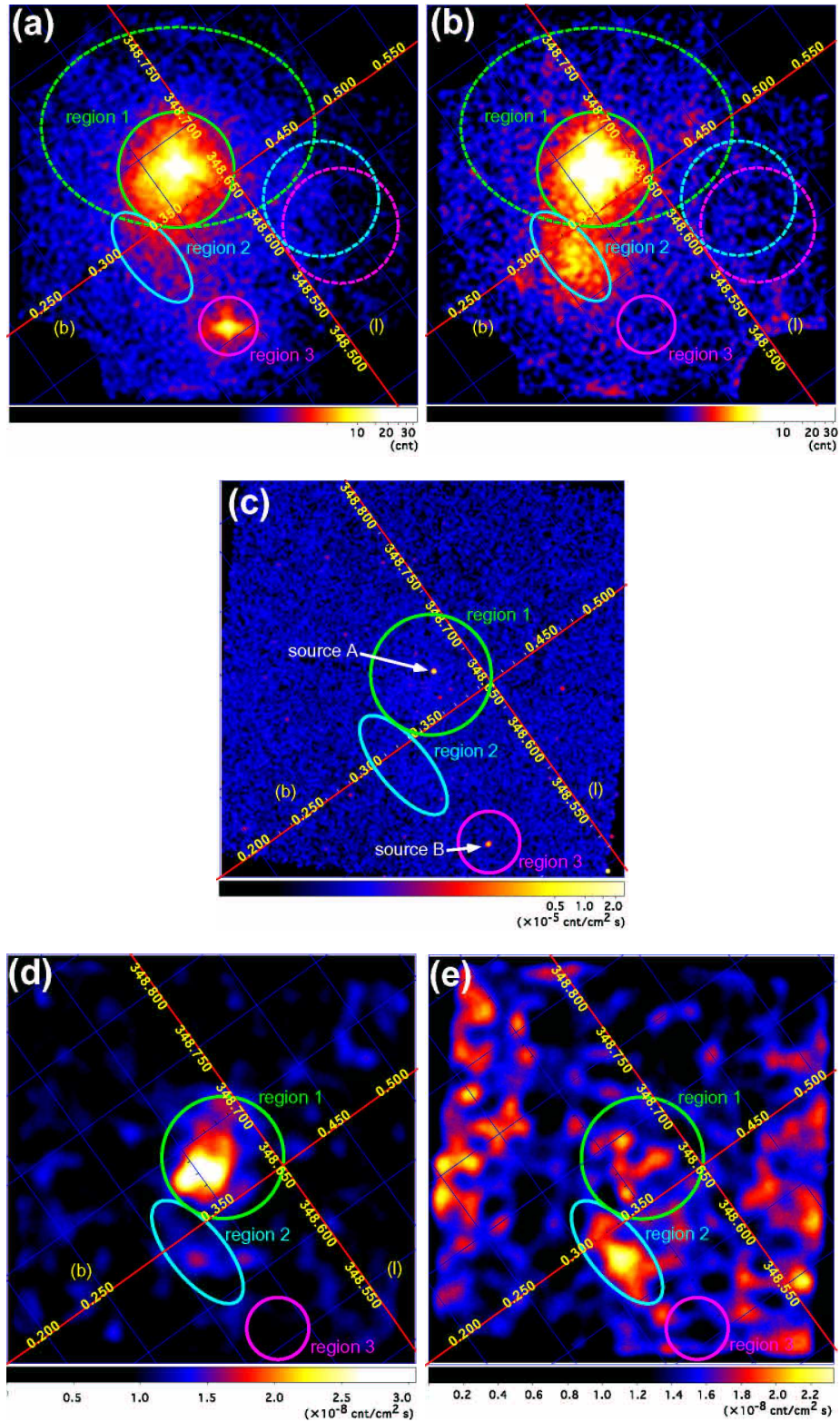


Fig. 1. Images of CTB37B in the galactic coordinates. Panels (a) and (b) are Suzaku images in 0.3–3.0 keV and 3.0–10.0 keV, respectively, which are smoothed with a Gaussian with $\sigma = 12$ arcsec. Panel (c) is the Chandra image in the 0.3–10.0 keV band being smoothed with a Gaussian with $\sigma = 6$ arcsec. Panels (d) and (e) are the Chandra images in 0.3–3.0 keV and 3.0–10.0 keV, respectively. After removing point sources, we smoothed them with a Gaussian with a σ of 40 arcsec. Solid circles in green, blue, and magenta are the integration region of source photons which are named as region 1 through 3 in this order. Region 1 is a circle with a radius of $2/6$, region 2 is an ellipse with a size of $1/1 \times 2/5$, and region 3 is a circle with a radius of $1/3$. The dashed regions are corresponding background-integration regions.

Table 1. Count rates of sources and diffuse emission of Chandra data.

Region	Energy band	Point source count rate *	Diffuse emission count rate *
		[10^{-2} counts s^{-1}]	[10^{-2} counts s^{-1}]
region 1	0.3–3.0 keV	2.7 ± 0.1	3.3 ± 0.2
	3.0–10.0 keV	2.4 ± 0.1	0.64 ± 0.26
	total	5.0 ± 0.1	3.9 ± 0.4
region 2	0.3–3.0 keV	—	0.43 ± 0.15
	3.0–10.0 keV	—	0.93 ± 0.19
	total	—	1.4 ± 0.2
region 3	0.3–3.0 keV	2.3 ± 0.1	—
	3.0–10.0 keV	0.024 ± 0.021	—
	total	2.3 ± 0.1	—

Note — All errors are at 1σ confidence level.

1RXS J171354.4–381740) locating at $(l, b) = (348.^{\circ}561, 0.^{\circ}332)$, and no diffuse emission is associated in 0.3–3.0 keV and 3.0–10.0 keV band. Table 1 summarizes the background subtracted source count rates separately for point and diffuse sources in region 1, region 2 and region 3.

3.3. Correlation with Other Energy Band

Fig. 2 shows brightness contours of radio at 1.4 GHz in blue and of TeV γ -ray with H.E.S.S. in green, overlaid on the gray scale image of the Suzaku in the 0.3–10.0 keV band. Source A and B resolved by Chandra are represented by the filled red boxes. The radio image is taken from the NRAO

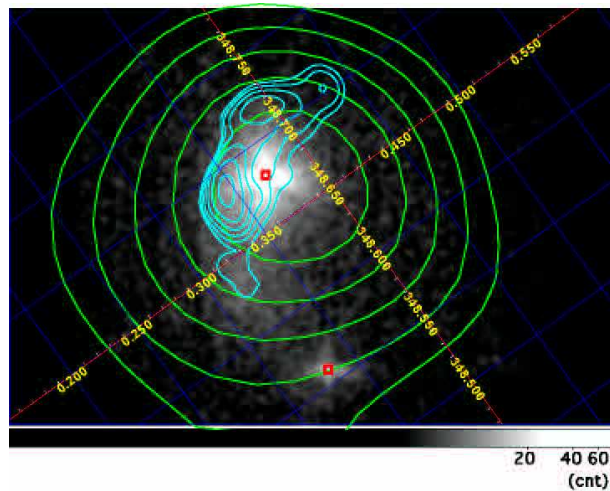


Fig. 2. Gray scale Suzaku X-ray image with radio and TeV γ -ray contours (blue and green, respectively) overlaid. The blue radio contours are in logarithmic scale from 0.016 to 1.3 Jy/beam. The green TeV contours are in linear scale from 30 to 50 count/ 0.9 arcmin^2 stepped by 4. Red boxes are source A and B, and green cross is the center of TeV γ -ray emission.

VLA Sky Survey (NVSS) database¹ (Condon et al. 1998). The X-ray emission well conforms with the shell in radio. Particularly, the diffuse X-ray source detected by Suzaku in region 2 is associated with the southern radio sub-peak. On the other hand, the peak of TeV γ -ray emission and source A seems to be separated from the radio shell. Note, however, that, due to limited spatial resolution of H.E.S.S., the apparent TeV source morphology is consistent with that of the radio shell whose radius is 4'.5 (Aharonian et al. 2008).

4. Spectral Analysis

In this section, we present results of spectral analysis of the three regions described above. We adopt the metal composition of Anders & Grevesse (1989) as the solar abundance. Spectral fits are carried out with XSPEC. We always adopt an ancillary response file (ARF) for a point source, since the sizes of region 1 and 2 are so small that the resultant spectral parameters including the flux will differ only by $\sim 1\%$ from the case if we take into account the spatial extent. The errors quoted are always at the 90% confidence level.

4.1. Region 1

The Chandra spectrum of source A is shown in Fig. 3(a). In extracting this spectrum, we took a circular integration region with a radius of 3'' centered at the source. We made no background subtraction. Since there is no apparent emission lines, we attempted to fit a power-law model undergoing photoelectric absorption (“phabs” model in XSPEC) to the spectrum. The best-fit model is overlaid in the upper panel of Fig. 3(a) as the histogram. The best-fit parameters are summarized in table 2. The photon index, the hydrogen column density, and the intrinsic flux in the 2.0–10.0 keV band are $3.2_{-0.3}^{+0.4}$, $4.0 (\pm 0.6) \times 10^{22} \text{ cm}^2$, and $1.8 (\pm 0.2) \times 10^{-12} \text{ ergs cm}^{-2}\text{s}^{-1}$, respectively, which are consistent with those of Aharonian et al. (2008).

Fig. 3(b) is the background-subtracted spectrum of Suzaku region 1. The black and red crosses represent the data points from the sum of the FI CCDs and those of the BI CCD, respectively. Although there is no sign of Fe $K\alpha$ line in the 6–7 keV band, we have obviously detected $K\alpha$ emission lines from He-like Mg (1.34 keV), Si (1.86 keV), and S (2.46 keV) as well as a $K\beta$ emission line from He-like Si (2.18 keV). This means that the spectrum includes a thermal emission component. We thus tried to fit the Suzaku spectrum with a model composed of a power law representing source A and a non-equilibrium collisional ionization plasma emission model (“vnei” model in XSPEC; Borkowski et al. 2001; Hamilton et al. 1983; Borkowski et al. 1994; Liedahl et al. 1995) undergoing photoelectric absorption with a common N_{H} . In the fitting, we set abundances of Mg, Si, and S free to vary. The other abundances are fixed as solar abundance. The best-fit parameters are summarized in Table 2, and the best-fit models are displayed in Fig. 3(b). The fact that no iron $K\alpha$ emission line was detected can be attributed that the non-thermal component dominates the spectrum in the energy band above 3 keV. The reduced χ^2 of 1.06 implies that the fit is acceptable at the 90%

¹ <http://www.cv.nrao.edu/nvss/>

confidence level. The temperature and the ionization parameter of the “vnei” component are obtained to be $kT = 0.89_{-0.17}^{+0.22}$ keV and $n_e t [\text{cm}^{-3}\text{s}] = 3.5_{-1.1}^{+13} \times 10^{10}$, respectively. On the other hand, the photon index of the power-law model is $\Gamma = 3.0 \pm 0.2$ and the intrinsic flux is $3.3_{-0.4}^{+0.3} \times 10^{-12}$ ergs $\text{cm}^{-2}\text{s}^{-1}$. The photon index is consistent between Suzaku and Chandra, whereas the flux with Suzaku seems to be greater than that with Chandra by a factor of ~ 1.8 . We remark that, since there is no sign of emission lines in the Chandra spectrum of source A, the thermal component should be extended.

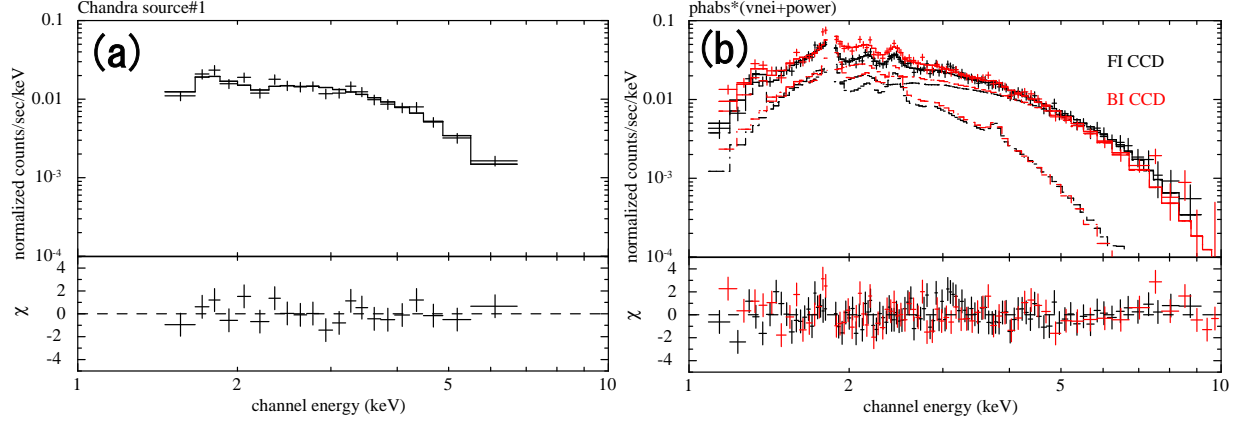


Fig. 3. (a) Chandra spectrum integrated from a circular region with a radius of $3''$ centered on source A. The best-fit model represented by a power law (histogram) is overlaid. (b) Suzaku spectra of region 1 from the FI-CCDs (black) and the BI-CCD (red) with a model composed of a “vnei” and a power law model. The best-fit parameters are summarized in table 2.

4.2. Region 2

The Suzaku spectra of region 2 together with best-fit model and residual are shown in Fig. 4. The basic features such as the He-like Si $K\alpha$ emission line and no apparent sign of Fe emission line are

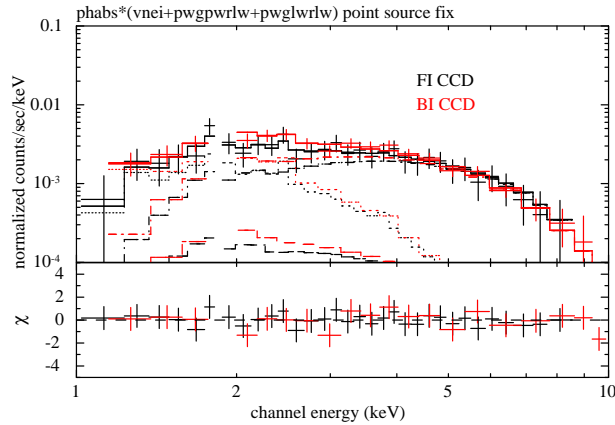


Fig. 4. The XIS spectra of region 2 with a model composed of a “vnei” and two power-law components, of which one represents contamination from source A. The normalization of “vnei” model and all parameters of the other power law are set free to vary.

Table 2. Best-fit parameters of the region 1 spectra

Parameters	Chandra source A	Suzaku
Power Law		
Photon Index	$3.2^{+0.4}_{-0.3}$	3.0 ± 0.2
Intrinsic Flux ^a	1.8 ± 0.2	$3.3^{+0.3}_{-0.4}$
VNEI		
Temperature [keV]	...	$0.89^{+0.21}_{-0.17}$
abundance ^b Mg	...	$0.61^{+0.31}_{-0.19}$
Si	...	$0.40^{+0.21}_{-0.14}$
S	...	1.0 ± 0.6
$n_e t$ ^c	...	$3.5^{+13}_{-1.1}$
$E.M.$ ^d	...	$2.1^{+1.6}_{-1.0}$
N_H ^e	4.0 ± 0.6	$3.6^{+0.4}_{-0.2}$
$\chi^2/\text{d.o.f}$	14.6/18	176.1/166

^a Flux in the 2.0–10.0 keV band in the unit of 10^{-12} ergs cm^{-2} s^{-1} .

^b Abundance ratio relative to the solar value (Anders & Grevesse, 1989).

^c Ionization time-scale in the unit of 10^{10} s cm^{-3} , where n_e and t are the electron density and age of the plasma.

^d Emission measure $E.M. = \int n_e n_H dV \simeq n_e^2 V$ in the unit of 10^{58} cm^{-3} , where n_e and V are the electron density and the plasma volume. The distance to CTB37B is assumed to be 10.2 kpc (Caswell et al. 1975)

^e Absorption column density in the unit of 10^{22} cm^{-2} .

similar to those in region 1. In addition to the thermal and non-thermal components, we need to take into account possible contamination from source A which is brightest in region 1. In fitting the region 2 spectra, we thus first tried a “vnei + power law (1) + power law (2)” model, where the power law (1) accounts for the source A contamination, and the power law (2) represents a non-thermal component dominating the high energy band image in region 2 (Fig. 1). The vnei component, on the other hand, represents the contamination from region 1, and intrinsic thermal emission from region 2 if any. Note that the region 2 spectra are statistically poorer than those of region 1. Hence we have fixed the temperature, the abundances of Mg, Si, and S, the ionization parameter of the vnei component and the photon index of power law (1) at the best-fit values obtained in the region 1 fit, which are summarized in table 2. The flux between 2.0–10.0 keV of power law (1) is fixed at 3.3×10^{-14} ergs cm^{-2} s^{-1} , which is $\sim 1\%$ of the source A flux, on the basis of the vignetting function (Serlemitsos et al. 2007). As a result, the free parameters are the hydrogen column density, the normalization of the vnei component, and all parameters of power law (2). The result of the fit is shown in Fig. 4, and the best-fit parameters are summarized in table 3. The $E.M.$ of the vnei component is ~ 11 (4-20) % of the region 1 best-fit value. On the other hand, we simulated the contamination of the vnei component from region 1 using

smoothed Chandra image, and found the contamination is $\sim 7\%$. The thermal component apparent in region 2 spectra can therefore be entirely regarded as the contamination from region 1, and the upper limit of the $E.M.$ intrinsic to region 2 is 13% of that of region 1, or $2.7 \times 10^{57} \text{ cm}^{-3}$. The photon index of power law (2) results in $\Gamma = 1.5 (\pm 0.4)$ with the reduced χ^2 of 0.36. It is remarkable that the X-ray photon index $\Gamma = 1.5$ is consistent with the standard radio energy index of non-thermal SNRs $\alpha = 0.5$.

We next replaced the power-law (2) component by an ‘‘srcut’’ model, which simulates a synchrotron spectrum from an exponentially cut off power-law distribution of electrons in a homogeneous magnetic field (Reynolds 1998; Reynolds & Keohane 1999). According to the Green’s catalogue², the radio spectral index (α) is 0.3 with a flux at 1 GHz of 26 Jy. This small index, however, is probably due to contamination of thermal emission. A similar situation has been reported for 30 Dor C (Smith & Wang 2004). We thus fixed α at 0.5, which is the typical value of the SNRs in the radio band, and set the flux at 1 GHz free to vary. As a result, the normalization of the srcut model is obtained to be 1.43 mJy at 1 GHz. This is much smaller than the radio flux 26 Jy at 1 GHz. Note, however, that this radio normalization is an integration of the entire radio image of CTB37B, part of which is, however, spilt out of regions 1 and 2. Moreover, the radio flux encompassed in region 2 is only $\approx 2\%$ of that in region 1. We therefore estimate the radio flux within region 2 to be $\approx 1\%$ of the total, or ≈ 300 mJy at 1 GHz. Even after this correction, simple extrapolation of the srcut model well fit to the X-ray spectra to the radio band is much smaller than the observed radio flux. We guess that the flux in the radio band is dominated by thermal emission. The resultant normalization (emission measure) of the vnei component does not change within the error. The reduced χ^2 value is nearly the same as that of the power-law fit. The lower limit of the roll-off energy is obtained to be 14.8 keV. We confirmed that the roll-off energy does not change drastically if we varied α in the range 0.3–0.7. Based on these results, it is possible to interpret that the spectrum of the non-thermal component extends from X-ray to radio with an energy index of 0.5 in the radio band.

4.3. Region 3

Fig. 5 shows the background-subtracted spectra of region 3. As indicated by the images in Fig. 1(a), X-ray flux is detected only below ~ 3 keV. Since the absorption is apparently weak and there is Fe-L hump in the 0.7–0.9 keV band, this source seems to be a foreground point source, probably an active star. We thus adopted a model composed of a thin thermal collisional equilibrium plasma emission model (‘‘mekal’’ model in XSPEC; Mewe et al. 1985; Mewe et al. 1986; Liedahl et al. 1995; Kaastra et al. 1996) multiplied by photoelectric absorption, and fitted this model to the spectra in the 0.5–2.0 keV band. The result is shown in Fig. 5, and the best-fit parameters are listed in Table 4. Note that the fit residuals exhibit different behavior in the 0.7–1.0 keV band between the FI and BI CCDs. This is probably attributed to calibration uncertainty.

² <http://www.mrao.cam.ac.uk/surveys/snrs/>

Table 3. Best-fit parameters of the region 2 spectrum

Parameters	VNEI + Powerlaw + Powerlaw	VNEI + Powerlaw + srcut
VNEI		
Temperature [keV]	0.89 (fix)	0.89 (fix)
abundance ^a Mg	0.61 (fix)	0.61 (fix)
Si	0.40 (fix)	0.40 (fix)
S	1.0 (fix)	1.0 (fix)
$n_e t$ ^b	3.5 (fix)	3.5 (fix)
$E.M.$ ^c	$0.23^{+0.18}_{-0.15}$	$0.23^{+0.14}_{-0.15}$
Power Law (1)		
Photon Index	3.0 (fix)	3.0 (fix)
Intrinsic Flux ^d	0.033 (fix)	0.033 (fix)
Power Law (2)		
Photon Index	1.5 ± 0.4	...
Intrinsic Flux ^d	$0.78^{+0.07}_{-0.08}$...
srcut		
alpha	...	0.5 (fix)
roll-off E [keV]	...	>14.8
Normalization ^d	...	1.4
Intrinsic Flux ^e	...	0.78
phabs N_H ^f	$3.5^{+0.5}_{-0.7}$	$3.5^{+0.5}_{-0.7}$
$\chi^2/\text{d.o.f}$	17.5/48	17.5/48

^a Abundance ratio relative to the solar value (Anders & Grevesse, 1989).

^b Ionization time-scale in the unit of $10^{10} \text{ s cm}^{-3}$, where $n_e t$ and t are the electron density and age of the plasma.

^c Emission measure $E.M. = \int n_e n_H dV \simeq n_e^2 V$ in the unit of 10^{58} cm^{-3} , where n_e and V are the electron density and the plasma volume. The distance to CTB37B is assumed to be 10.2 kpc (Caswell et al. 1975)

^d Radio flux at 1 GHz in the unit of 10^{-3} Jy .

^e Flux in the 2.0–10.0 keV band in the unit of $10^{-12} \text{ ergs cm}^{-2} \text{ s}^{-1}$.

^f Absorption column in the unit of 10^{22} cm^{-2} .

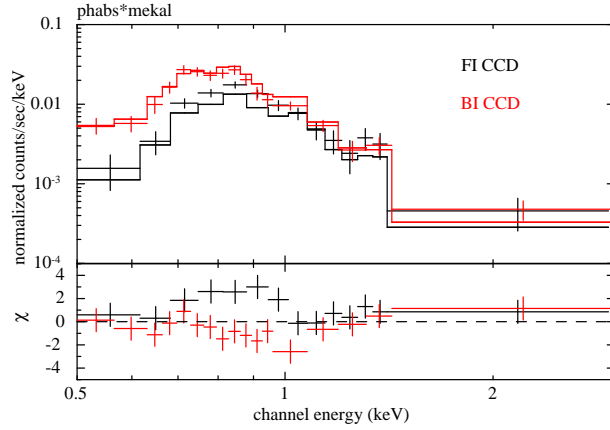


Fig. 5. The XIS spectra of region 3 with the MEKAL model.

Table 4. Best-fit parameters of the region 3 spectrum

MEKAL	
Temperature [keV]	$0.46^{+0.03}_{-0.05}$
Abundance ^a	$0.20^{+0.12}_{-0.07}$
Normalization ^b [cm ⁻³]	$2.5^{+1.4}_{-0.6} \times 10^{-4}$
phabs	
N_{H} ^c	<0.046
$\chi^2/\text{d.o.f}$	52.9/27

^a Abundance ratio relative to the solar value (Anders & Grevesse, 1989).

^b Normalization is $\frac{10^{-14}}{4\pi D_A^2} \int n_e n_H dV$ where D_A is the angular size distance to the source (cm), n_e and V are the electron density and the plasma volume.

^c Absorption column in the unit of 10^{22} cm⁻².

5. Timing Analysis

In order to understand the nature of the point sources, we carried out timing analysis.

5.1. Source A

We searched the Chandra data for a pulsation from source A. Unfortunately, source A locates close to the chip boundaries of the ACIS-I, and is affected by the instrumental dithering effects. In fact, the source drops into the boundary every 1000 s, during which the source count diminishes significantly. Removing these time intervals with a Good Time Interval filtering, we made a light curve and search for a pulsation. The power spectrum on the basis of a 3.2 s binning light curve in the 0.3–10 keV band is shown in Fig. 6. We do not detect any pulsation in the period range between 6.6–3000 s.

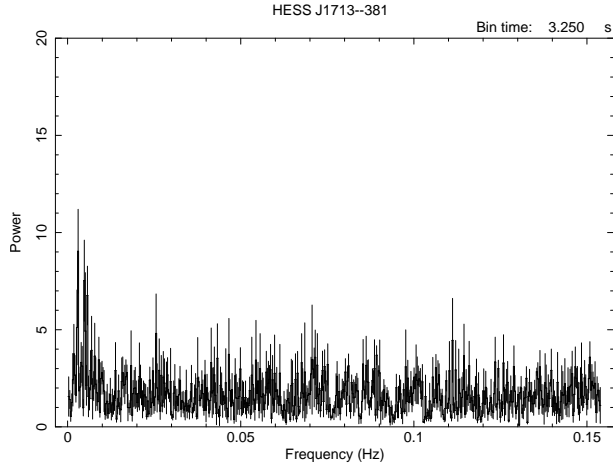


Fig. 6. Power spectrum of source A in the 0.3–10.0 keV band with the time bin size of 3.2 sec.

5.2. Source B

We created a light curve of source B in the 0.5–2.0 keV band with Suzaku, which is shown in Fig. 7. The time bin size is 512 s. Although we detected no drastic flare event, the light curve seems

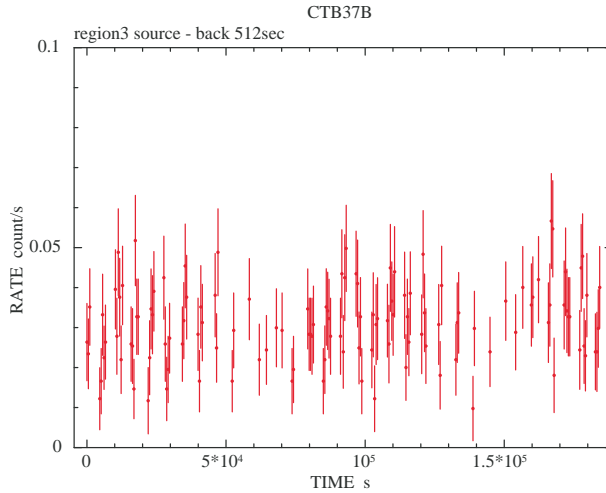


Fig. 7. The light curve of region 3 in the 0.5–2.0 keV band. The time bin size is 512 s.

to show flickering. In fact, Kolmogorov–Smirnov test indicates the probability of no variability in the light curve is 0.0012.

6. Discussion

6.1. Thermal Component

We have calculated the electron number density and the age of the diffuse thermal plasma of region 1 and 2 on the basis of the best-fit parameters summarized in table 2 and 3. We assume that the plasma in region 1 distributes uniformly within a sphere with a radius of $1'4$, which is the

Half-Width-of-Half-Maximum (HWHM) radius obtained from the Chandra image (Aharonian et al. 2008). Assuming the distance to CTB37B of 10.2 kpc (Caswell et al. 1975), we obtain the real radius of region 1 to be $r_{\text{reg1}} = 1.3 \times 10^{19}$ cm. Accordingly, the volume of the region 1 plasma is $V_{\text{reg1}} = (4/3)\pi r_{\text{reg1}}^3 = 9.2 \times 10^{57}$ cm³. In the same way, from HWHM of an estimated image size of $1'.9 \times 0'.9$, the real length of semi-major and semi-minor axes result in $r_{\text{reg2,l}} = 1.7 \times 10^{19}$ cm and $r_{\text{reg2,s}} = 8.2 \times 10^{18}$ cm, respectively. Assuming that the line-of-sight extent of region 2 is $r_{\text{reg2,s}}$, the volume of region 2 is calculated to be $V_{\text{reg2}} = (4/3)\pi r_{\text{reg2,l}} r_{\text{reg2,s}}^2 = 4.8 \times 10^{57}$ cm³ (the resultant electron density becomes smaller by a factor of $\sqrt{2}$ if we substitute $r_{\text{reg2,l}}$ for $r_{\text{reg2,s}}$). With the aid of the emission measures obtained from the spectral fitting, $E.M. = \int n_e n_H dV = 2.1_{-1.0}^{+1.6} \times 10^{58}$ cm⁻³ (region 1) and 2.6×10^{57} cm⁻³ (region 2 upper limit, see § 4.2), the electron number density of region 1 and 2 are

$$n_{e,\text{reg1}} = 1.7 (1.2 - 2.2) [\text{cm}^{-3}]$$

and

$$n_{e,\text{reg2}} \leq 0.82 [\text{cm}^{-3}],$$

where we adopt the relation $n_e \approx 1.24 n_H$ for fully ionized plasma. The parameter region in parenthesis is those allowed at the 90% confidence level. Assuming the strong shock, we obtain the pre-shock densities to be ~ 0.43 cm³ and $\lesssim 0.21$ cm³, respectively, which are significantly lower than the average density of the interstellar matter in the galactic plane. That means CTB37B exploded in a low density space. The density of region 1 together with the ionization parameter obtained from the fit of the region 1 spectra $n_{e,\text{reg1}} t = 3.5_{-1.1}^{+1.3} \times 10^{10}$ [cm⁻³ s], enables us to estimate the age of the plasma observationally for the first time as

$$t_{\text{reg1}} = 6.5 (3.7 - 31) \times 10^2 [\text{yr}].$$

CTB37B is one of the best candidates of SN393 in Chinese historical record (Stephenson & Green 2002). The plasma age calculated from the observed ionization parameter and emission measure supports this identification.

The number of electrons ($N_e = n_e V$) in region 1 and 2 are $N_{e,\text{reg1}} = 1.6 (1.1 - 2.0) \times 10^{58}$ and $N_{e,\text{reg2}} \leq 3.9 \times 10^{57}$. As a result, the total mass included in the two regions are $15 (11-20) M_\odot$ and $\leq 3.7 M_\odot$, respectively, and the thermal energy ($E = \frac{3}{2}(N_e + N_H + N_{\text{He}})kT$) are

$$E_{\text{reg1}} = 6.4 (4.1 - 8.6) \times 10^{49} [\text{ergs}]$$

$$E_{\text{reg2}} \leq 1.6 \times 10^{49} [\text{ergs}].$$

under the assumption of energy equipartition between electrons and ions. The total thermal energy could be larger if other portions of the remnant are included and if the proton temperature is significantly larger than the electron temperature as is expected for supernova remnants with large shock velocities (Ghavamian et al. 2007).

6.2. The Nature of the Point Sources

6.2.1. Source A

The best-fit spectral parameters of Chandra source A and those of Suzaku region 1 (source A and the diffuse thermal emission) are summarized in table 2. The measured hydrogen column densities ($N_{\text{H}} \simeq 4 \times 10^{22} \text{ cm}^{-2}$) are the same between Chandra and Suzaku. However, since the Suzaku spectra below ~ 1 keV is dominated by the diffuse thermal component (Fig. 3), N_{H} obtained with Suzaku is determined mainly by the diffuse emission. This implies that source A is probably associated physically with the diffuse thermal emission in region 1, and is most likely a neutron star (or a black hole) born with the supernova explosion leading to CTB37B. In fact, the large photon index of 3.2 and luminosity of $2.2 \times 10^{34} \text{ ergs s}^{-1}$ are both consistent with those of anomalous X-ray pulsar (AXP; Fahlman & Gregory 1981; Kuiper et al. 2006). Young age of ~ 700 yr (§ 6.1) also supports this interpretation (*e.g.* the AXP 1E1841-045 is associated with Kes 73 whose age is estimated to be 500-1000 yr; Tian & Leahy 2008). Since the spin period of AXP is in the range 6–12 s, it is natural that we have found no evidence of pulsation from the Chandra data, because the frame time of the ACIS-I is 2.3 s. In addition, the flux of the power law measured by Suzaku is apparently greater than that with Chandra by a factor of 1.8 (§4.1, table 2). Note that the point spread function of the Suzaku XRTs is not so sharp. Hence one may doubt that part of the power-law flux detected by Suzaku can be attributed to a putative diffuse non-thermal emission. However, $\sim 80\%$ of the Chandra region 1 photons above 3 keV, where the power-law component is dominant in the Suzaku spectra (see Fig. 3), originates from source A (table 1). Since the diffuse emission occupies only a small fraction in region 1, the flux difference between Chandra and Suzaku cannot be explained unless source A has really varied. This kind of long term variation is detected also from some other AXPs (Gavriil & Kaspi 2002; Kaspi et al. 2003). We therefore conclude based on the Chandra and Suzaku observations that source A is probably a new AXP. We need a fast timing observation with an imaging detector with a time resolution of less than 1 s to confirm our conclusion.

6.2.2. Source B

From the spectrum fitting, The hydrogen column density obtained from the fit to the Suzaku region 3 spectra $N_{\text{H}} < 4 \times 10^{20} \text{ cm}^{-2}$ (table 4) is much smaller than that obtained from region 1 and 2. This result indicates that source B is a foreground source. The best-fit plasma temperature of $kT \simeq 0.5$ keV is reminiscent of an active star. The existence of flickering (§5.2) supports this suggestion.

6.3. Non-Thermal Component

X-ray emission from CTB37B is composed of the diffuse thermal component (region 1) and the non-thermal component (region 2) as well as a point source (source A), as demonstrated in §3 and §4. Hence, CTB37B now is the third SNR after RCW86 and Cas A that possesses the thermal and non-thermal X-ray emissions and TeV γ -ray emission all together. In addition, CTB37B is now the fifth SNR, following RCW86, Cas A, RX J1713.7–3946 and Vela Jr., from which non-thermal

Table 5. Comparison of non-thermal component with other SNRs.

Target Name	L_x *	L_{TeV} †	L_{TeV}/L_x	Γ_x	Γ_{TeV}	References ‡
CTB37B (region 2)	0.97	0.59 §	0.61	1.5	2.3	(1)
RCW86	3.8	0.55	0.14	3.1	2.5	(2)(3)
Cas A	110	0.21	0.0019	3.1	2.4	(4)(5)
RXJ1713	6.5	0.42	0.06	2.4	2.2	(6)(7)
VELA Jr.	$\sim 1.5 \times 10^{-2}$	0.033	~ 2.2	2.6	2.1	(8)
SN1006	2.1	<0.15	<0.1	2.7	...	(9)(10)

* Unabsorbed flux in the 2–10 keV band in the unit of 10^{34} ergs s^{-1} .

† Unabsorbed flux in the 1–10 TeV band in the unit of 10^{34} ergs s^{-1} .

‡ (1) Aharonian et al. (2006); (2) Bamba et al. (2000); (3) Hoppe et al. (2007); (4) Helder et al. (2008);

(5) Albert et al. (2007); (6) Slane et al. (1999); (7) Aharonian et al. (2004); (8) Aharonian et al. (2005);

(9) Bamba et al. (2008); (10) Aharonian et al. (2005b)

§ TeV γ -ray flux contributed to region 2 was calculated as a quarter of the total flux.

radiation is detected both in X-ray and TeV γ -ray bands. The fluxes of the non-thermal emission of these five non-thermal SNRs are compared in table 5. The non-thermal diffuse component detected from region 2 has a remarkably flat X-ray spectrum with a photon index of 1.5. Since this photon index is equal to the typical radio photon index (energy index $\alpha = 0.5$), the non-thermal emission spectrum can be considered as extending from the radio band smoothly to the X-ray band, thereby the roll-off energy results in as high as $\gtrsim 15$ keV (table 3). This roll-off energy is higher than any other SNR that is accompanied by the non-thermal X-ray and TeV γ -ray emission, such as $\lesssim 9$ keV for RX J1713.7–3946 (Takahashi et al. 2008), ~ 0.23 keV for SN1006 (Bamba et al. 2008), ~ 0.87 keV for RCW 86 (Bamba et al. 2005). This indicates high electron acceleration efficiency in region 2. In addition, the density around region 2 is considered as being lower than in region 1, given that only the upper limit of the thermal emission is obtained (§ 6.1). The lower density may indicate higher shock velocity due to the smaller deceleration, which is consistent with the fact that the roll-off frequency is proportional to the square of the shock velocity (Aharonian & Atoyan 1999).

It should be a matter of debate whether the TeV γ -ray emission and the non-thermal X-ray emission from region 2 are produced by the same population of electrons, since the images of these two bands shown in Fig. 2 are far from similar at first sight. The TeV γ -ray image is compatible with a shell with a radius of $\sim 4' - 6'$ due to limited spatial resolution of H.E.S.S. (Aharonian et al. 2008), which is compatible with the size of the radio shell. We thus assume that the TeV γ -ray emission is powered through 1-Zone Inverse Compton scattering (IC) of the cosmic microwave background due to the accelerated electrons.

The maximum electron energy (E_{\max}) can be evaluated by the shape of TeV γ -ray spectrum. Using the H.E.S.S. spectrum whose photon index is 2.3 (Aharonian et al. 2006) shown in Fig. 8 in blue, we determined E_{\max} of 10 TeV. The red line in Fig. 8, on the other hand, is the X-ray power-law spectrum of region 2 with a photon index of 1.5. A series of the dashed plots are the model spectra

calculated under the assumptions of E_{\max} of 10 TeV, an index of the electron energy distribution of 2, and various magnetic field (0.1, 1.0 and 10.0 μG). It is clear from this figure that 1-zone IC model is unable to explain the synchrotron X-ray spectrum with any magnetic field strength. This suggests that TeV γ -ray emission is due to multi-zone IC scattering, or the decay of neutral pions generated by the high energy proton impacts.

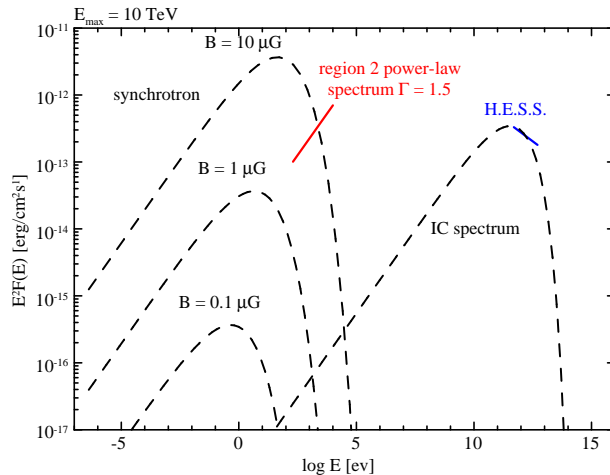


Fig. 8. Spectrum energy distribution of region 2 from the X-ray and TeV γ -ray bands. The dashed plots on the left are the synchrotron radiation models with various magnetic field, and on the right is IC model spectrum. All the curves assume the maximum energy of electrons of 10 TeV. Blue line is the spectrum from H.E.S.S. observation ($\Gamma = 2.3$; Aharonian et al. 2006), and the red line is the Suzaku region 2 spectrum which is a power law with $\Gamma = 1.5$.

7. Conclusion

We have obtained with Suzaku the images and the high quality spectra of the supernova remnant CTB37B. The X-ray diffuse emission region coincides with that of radio and TeV γ -ray. The X-ray emission consists of thermal and non-thermal diffuse components as well as a point source resolved by Chandra. CTB37B is the third SNR from which thermal and non-thermal X-ray emissions as well as TeV γ -ray emission are detected all together, and the fifth SNR that is accompanied by non-thermal emission both in X-ray and TeV γ -ray bands.

The diffuse thermal emission can be best described by a non-equilibrium collisional ionization plasma model (NEI model) with a temperature, an ionization parameter ($n_e t$ [cm^{-3}s]), and the abundances of 0.9 ± 0.2 keV, $3.5^{+13}_{-1.1} \times 10^{10}$, and $\simeq 0.5 Z_{\odot}$ (Mg, Si), respectively. The image size and the observed emission measure provides the number density of the thermal electrons before the shock to be $0.2\text{--}0.4 \text{ cm}^{-3}$, which is significantly lower than that of the Galactic plane. This suggests that the supernova explosion associated with CTB37B took place at a low density space. From the ionization parameter and the number density of the thermal electron, the age of the plasma is found to be $\sim 650^{+2500}_{-300}$ yr. This is consistent with the tentative identification of CTB37B with SN393 within the error.

In contrast, the diffuse component occupying southern part of CTB37B (region 2) is non-thermal and represented by a power-law model or a srcut model. The photon index of 1.5 is significantly smaller than any other non-thermal SNR, but is consistent with that of a typical non-thermal SNR in the radio band. The srcut model fit with its normalization set free to vary therefore results in a high roll-off energy of >15 keV. Under the assumption that TeV γ -ray was emitted by 1-zone IC scattering, there are no solution for magnetic field strength that can reproduce the observed synchrotron spectrum in X-ray. This suggests that TeV γ -ray is produced by multi-zone IC scattering, or by the decay of neutral pions generated by the high energy proton impacts.

Owing to the high spatial resolution of Chandra, a point source is resolved from the brightest part of the Suzaku image of CTB37B (region 1). Its association to the diffuse thermal emission indicated by N_{H} , the photon index of ~ 3 , the X-ray luminosity of order 10^{34} erg s^{-1} , and the long term flux variation evident from the Chandra and Suzaku observations all indicate that the point source is a new anomalous X-ray pulsar. A high speed photometric observation is encouraged.

The authors are grateful to all of the Suzaku and H.E.S.S. team members. We also thank H. Yamaguchi, T. Tanaka and J. Vink for useful comments. This work was supported in part by Grant-in-Aid for Scientific Research of the Japanese Ministry of Education, Culture, Sports, Science and Technology, No. 19-4014 (A. B.), No. 18740153, No. 19047004 (R. Y.).

References

- Aharonian, F. A., Atoyan, A. M., & Kifune, T. 1997, MNRAS, 291, 162
Aharonian, F. A., & Atoyan, A. M. 1999, A&A, 351, 330
Aharonian, F. A., et al. 2004, Nature, 432, 75
Aharonian, F., et al. 2005, A&A, 437, L7
Aharonian, F., et al. 2005, A&A, 437, 135
Aharonian, F., et al. 2006, ApJ, 636, 777
Aharonian, F., et al. 2007, A&A, 472, 489
HESS Collaboration: F. Aharonian 2008, ArXiv e-prints, 803, arXiv:0803.0682
Albert, J., et al. 2007, A&A, 474, 937
Anders, E., & Grevesse, N. 1989, Geochim. Cosmochim. Acta, 53, 197
Bamba, A., Koyama, K., & Tomida, H. 2000, PASJ, 52, 1157
Bamba, A., Yamazaki, R., Yoshida, T., Terasawa, T., & Koyama, K. 2005, ApJ, 621, 793
Bamba, A., et al. 2008, PASJ, 60, 153
Borkowski, K. J., Sarazin, C. L., & Blondin, J. M. 1994, ApJ, 429, 710
Borkowski, K. J., Lyerly, W. J., & Reynolds, S. P. 2001, ApJ, 548, 820
Case, G. L., & Bhattacharya, D. 1998, ApJ, 504, 761
Caswell, J. L., Murray, J. D., Roger, R. S., Cole, D. J., & Cooke, D. J. 1975, A&A, 45, 239
Condon, J. J., Cotton, W. D., Greisen, E. W., Yin, Q. F., Perley, R. A., Taylor, G. B., & Broderick, J. J. 1998, AJ, 115, 1693

Fahlman, G. G., & Gregory, P. C. 1981, *Nature*, 293, 202

Frail, D. A., Goss, W. M., Reynoso, E. M., Giacani, E. B., Green, A. J., & Otrupcek, R. 1996, *AJ*, 111, 1651

Gavriil, F. P., & Kaspi, V. M. 2002, *ApJ*, 567, 1067

Ghavamian, P., Laming, J. M., & Rakowski, C. E. 2007, *ApJL*, 654, L69

Hamilton, A. J. S., Chevalier, R. A., & Sarazin, C. L. 1983, *ApJS*, 51, 115

Helder, E. A., & Vink, J. 2008, *ArXiv e-prints*, 806, arXiv:0806.3748

Hoppe, S., Lemoine-Goumard, M., & for the H. E. S. S. Collaboration 2007, *ArXiv e-prints*, 709, arXiv:0709.4103

Ishisaki, Y., et al. 2007, *PASJ*, 59, 113

Kaastra, J. S., Mewe, R., & Nieuwenhuijzen, H. 1996, *UV and X-ray Spectroscopy of Astrophysical and Laboratory Plasmas*, 411

Kaspi, V. M., Gavriil, F. P., Woods, P. M., Jensen, J. B., Roberts, M. S. E., & Chakrabarty, D. 2003, *ApJL*, 588, L93

Kassim, N. E., Weiler, K. W., & Baum, S. A. 1991, *ApJ*, 374, 212

Kokubun, M., et al. 2007, *PASJ*, 59, 53

Koyama, K., Petre, R., Gotthelf, E. V., Hwang, U., Matsuura, M., Ozaki, M., & Holt, S. S. 1995, *Nature*, 378, 255

Koyama, K., Kinugasa, K., Matsuzaki, K., Nishiuchi, M., Sugizaki, M., Torii, K., Yamauchi, S., & Aschenbach, B. 1997, *PASJ*, 49, L7

Koyama, K., et al. 2007, *PASJ*, 59, 23

Kuiper, L., Hermsen, W., den Hartog, P. R., & Collmar, W. 2006, *ApJ*, 645, 556

Liedahl, D. A., Osterheld, A. L., & Goldstein, W. H. 1995, *ApJL*, 438, L115

Makishima, K., et al. 1996, *PASJ*, 48, 171

Matsumoto, H., et al. 2007, *PASJ*, 59, 199

Mewe, R., Gronenschild, E. H. B. M., & van den Oord, G. H. J. 1985, *A&AS*, 62, 197

Mewe, R., Lemen, J. R., & van den Oord, G. H. J. 1986, *A&AS*, 65, 511

Milne, D. K., Goss, W. M., Haynes, R. F., Wellington, K. J., Caswell, J. L., & Skellern, D. J. 1979, *MNRAS*, 188, 437

Mitsuda, K., et al. 2007, *PASJ*, 59, 1

Ohashi, T., et al. 1996, *PASJ*, 48, 157

Reynolds, S. P. 1998, *ApJ*, 493, 375

Reynolds, S. P., & Keohane, J. W. 1999, *ApJ*, 525, 368

Reynoso, E. M., & Mangum, J. G. 2000, *ApJ*, 545, 874

Serlemitsos, P. J., et al. 2007, *PASJ*, 59, S9

Slane, P., Gaensler, B. M., Dame, T. M., Hughes, J. P., Plucinsky, P. P., & Green, A. 1999, *ApJ*, 525, 357

Smith, D. A., & Wang, Q. D. 2004, *ApJ*, 611, 881

Stephenson, F. R., & Green, D. A. 2002, *Unknown*,

Sugizaki, M., Mitsuda, K., Kaneda, H., Matsuzaki, K., Yamauchi, S., & Koyama, K. 2001, *ApJS*, 134, 77

Takahashi, T., et al. 2007, *PASJ*, 59, 35

Takahashi, T., et al. 2008, *PASJ*, 60, 131

Tanaka, Y., Inoue, H., & Holt, S. S. 1994, *PASJ*, 46, L37

Tian, W. W., & Leahy, D. A. 2008, *ApJ*, 677, 292

Voges, W., et al. 1999, *A&A*, 349, 389

Yamauchi, S., Ueno, M., Koyama, K., & Bamba, A. 2008, *PASJ*, submitted